ACS NANO

www.acsnano.org

ARTICLE

All-Dielectric Metasurface Fluorescence Biosensors for High-Sensitivity Antibody/Antigen Detection

Masanobu Iwanaga*

Cite This: https://dx.doi.org/10.1021/acsnano.0c07722

Read Online

ACCESS | Metrics & More | Article Recommendations | Supporting Information

ABSTRACT: Protein biomolecules are used as markers for various diseases and infections and are targets in biosensing research and development. One of the highest-sensitivity biosensing techniques is considered to be fluorescence (FL) sensing. However, to our knowledge, no study has shown that all-dielectric metasurfaces can contribute to highly sensitive FL sensing. Here, we introduce an efficient type of FL-sensing platforms and show that all-dielectric metasurface FL biosensors are able to directly detect a representative antibody, immunoglobulin G, at very small concentrations on the order of pg/mL or tens of femtomolars. Furthermore, it is shown that they work efficiently as an indirect detection platform for standard cancer marker antigens, such as carcinoembryonic antigens, at concentrations well below the medical diagnosis criterion at 5 ng/mL. Importantly, the metasurface biosensors simultaneously suppress inhomogeneous FL responses, exhibit high reproducibility, and retain sensitivity, even in human serum. These results indicate that the present metasurface FL biosensors provide a high-sensitivity practical platform, suggesting that they are a better option than the commercially standard of enzyme-linked immunosorbent assays.

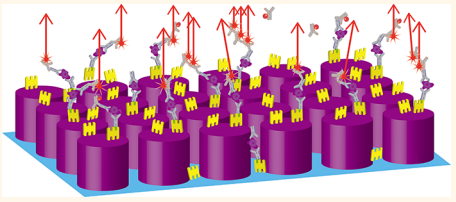

KEYWORDS: *all-dielectric metasurface, florescence biosensor, immunoglobulin G, p53 antibody, CEA*

Metasurfaces have been extensively investigated in recent years for conferring various optical functions to the artificially designed surfaces.[1−4] Most of the metasurface studies have been devoted to the manipulation of light waves regarding rays, phases, and holograms. Initially, plasmonic metasurfaces were mostly investigated, but gradually, all-dielectric metasurfaces have been attracting interest owing to the prominent optical resonances in the dielectric nanoresonators.[5]

Resonant wavelength shift has been reported in applications for biosensing on all-dielectric metasurfaces.[6,7] As the amount of immobilized target molecules increases, the resonant shift becomes larger. The principle underlying this effect is the same as that in surface plasmon resonance method.[8] To realize practical point-of-cure (POC) medical diagnosis, all-dielectric[6] and plasmonic[9] metasurfaces were coupled with microfluidic (MF) chips made of polydimethylsiloxane (PDMS). Cancer markers such as prostate specific antigen (PSA)[6] and carcinoembryonic antigen (CEA)[9,10] were detected in human serum with a total operation time of 3−5 h; the all-dielectric metasurfaces detected the target PSA of more than 1 ng/mL, which satisfies a diagnosis criterion of 4 ng/mL,[11] while the plasmonic metasurfaces detected the target CEA of more than 5 ng/mL, which needs an improvement in sensitivity to satisfy a diagnosis criterion of 5 ng/mL.[12−14] In the all-dielectric metasurfaces,[6,7] the limit of detection (LOD) of the target protein molecules by the resonant wavelength shift was approximately a few picomolars (pM) to tens of pM, taking into account the experimental configurations and conditions, whereas, in the plasmonic metasurfaces,[9,10] the LOD for CEA was approximately 30−60 pM. The LOD is less sensitive than that by commercially standard enzyme-linked immunosorbent assays (ELISA) that often claim to have a LOD of 1 pM or less; in the conventional ELISA, transmission at 450 nm is measured to evaluate the amount of enzyme products. The total operation time is typically 2−4 h, which is considered to be an issue and requires improvement.

One of the most sensitive biosensing techniques is fluorescence (FL) detection.[15] To date, it has been reported that the LOD using elaborate, costly, FL-detection setups reached a sub-femtomolar (fM) order (that is, 1 pg/mL or less) after the statistical analysis for antigen detection.[16−18] Apart

Received: September 14, 2020
Accepted: November 17, 2020

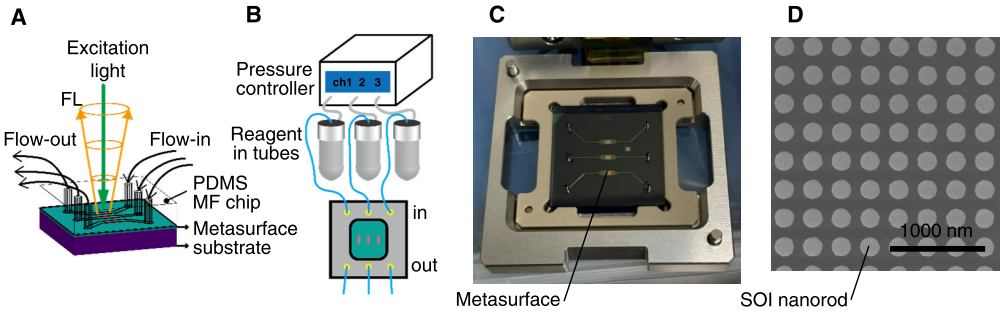

Figure 1. (A) Schematic illustration of the metasurface sensor chip, composed of a metasurface substrate (green and purple) and a PDMS MF chip (wire frame). (B) Schematic of the MF setup where the metasurface sensor chip is loaded in a holder. (C) Photograph of a metasurface chip set in the holder with the cover removed. The metasurface substrate was a 2 × 2 cm^2 square. (D) Top-view SEM image of the SOI-nanorod-array metasurface. The scale bar indicates 1000 nm.

from protein-molecule detection, FL-labeled DNA was sensitively detected; the target DNA of 5 fM was observed.[19]

Another approach to reach the extremely high sensitivity is to find excellent platforms for FL sensing. One of the candidates has been considered to be plasmonic nanostructures, which comprise metallic nanostructures. A report[20] claimed that the LOD using a plasmonic metasurface reaches a sub fM, concretely 30 attomolars, without relying on the costly setups.[16−18] Prominently FL-intensity-enhancing plasmonic metasurfaces[21−23] and plasmonic nanostructures on substrates,[24−27] which have similar capability to the plasmonic metasurface,[20] are reported so far; comparing them, thousand-fold FL-intensity enhancement was experimentally shown. The low reproducibility in most of the plasmonic platforms has been an issue when they are applied to practical biosensing. The highest reproducibility independent of incident light spots has been found only in the high-emittance-based metasurfaces;[22,23,28] the simultaneous highly FL-intensity enhancement and reproducibility were achieved by managing total FL processes of excitation, electronic transfer, and emission.[29]

In contrast to the plasmonic platforms,[18,20−27] highly FL-enhancing all-dielectric metasurfaces have hardly been reported. One exception is a metasurface of silicon-on-insulator (SOI) nanorod array,[30] which exhibits prominent FL-intensity-enhancing capability and is more than 1000-fold for that of a nonenhancing, flat silicon substrate. The FL-enhancement effect by the SOI-nanorod metasurfaces was quite reproducible. An advantage in all-dielectric metasurfaces is relatively simpler fabrication than the plasmonic metasurfaces without metal deposition;[20−23] therefore, lower cost is expected in practical applications. Another advantage in the all-dielectric metasurfaces is reusability by washing the metasurface substrates, as described later; this advantage will contribute to a substantial reduction of the running cost. In practical biosensing configurations, since the target molecules are not labeled, FL-labeled secondary antibodies (Abs) are added in a short operation time; the FL secondary Abs are widely available and an established tool in FL biosensing and bioimaging. This kind of demonstration is shown later, with setting the target to be CEA.

To make the best use of the metasurfaces as optical biosensors that can work in POC configurations, substantial changes in the setup are required because the quantitative control of several liquid reagents is necessary to make the metasurfaces quantitative biosensors. To address this issue, an experimental setup was prepared as follows.

Figure 1A schematically illustrates a metasurface sensor chip. A PDMS chip (wire frame) was self-absorbed on a metasurface substrate (green and purple) to form a metasurface sensor chip. The PDMS chip has in−out ports for the flow through liquid reagents, including biomolecules, and MF channels that are hundreds of micrometers in width and 30 μm in height.

As depicted in Figure 1B, the MF setup consists of a gas pressure controller, microtubes for liquid reagents, and a holder with in−out access to the metasurface chip. The flow rate of the reagents was quantitatively controlled and set to keep a range from 5 to 12 μL/min, in accordance with the molecular species. The metasurface chip was set in a holder, an image of which is shown in Figure 1C. Note that, although we here show the three-channel metasurface chip, it is certainly possible to extend the channel numbers. The three metasurface chips were placed at the center of the MF path. All-dielectric metasurfaces employed in this study comprised arrays of SOI nanorods.

To present an enlarged view of the metasurface, a top-view scanning-electron-microscopy (SEM) image of the metasurface is shown in Figure 1D. Scale bar indicates 1000 nm. The metasurface was designed to form a square lattice and have a periodicity of 300 nm and a nanorod diameter of 220 nm. The height of the nanorod was 200 nm. The SEM image shows that the nanofabrication was conducted as designed.

The metasurface sensor system was applied to detect Abs and antigens. The results are described in the following section, together with descriptions of the all-dielectric metasurfaces and the protocols for immobilizing binding molecules, targets, and the secondary Ab with FL labels. A representative Ab of immunoglobulin G (IgG) was very efficiently detected in a direct manner using the metasurface sensor system. In addition, to substantiate key properties as biosensors, specific detection was discriminated from nonspecific detection due to physical absorption and moreover was examined using human serum in target buffers. Furthermore, this study shows that, in a practical configuration called sandwich assay, a cancer marker antigen, CEA, was indirectly detected well below the medical diagnosis concentration. Specific details, such as model numbers of reagents and instruments, are compiled in the Methods.

RESULTS AND DISCUSSION

Optical Resonances in the SOI-Based Metasurfaces. Here, we address all-dielectric optical metasurfaces employed in the FL-sensing experiment. The structural design of the metasurfaces was optimized to realize the largest FL-intensity enhancement at 570−600 nm. Figure 2A shows the measured reflectance spectrum of the SOI-nanorod metasurface with a 400

https://dx.doi.org/10.1021/acsnano.0c07722
ACS Nano XXXX, XXX, XXX−XXX

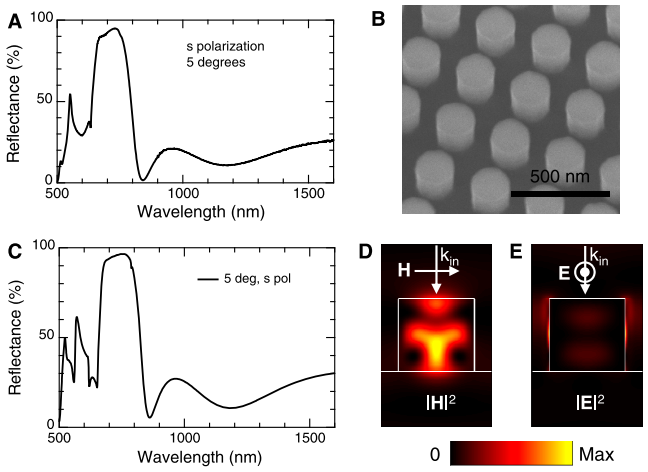

Figure 2. Optical resonances in the SOI-nanorod metasurface. (A) Measured reflectance spectrum at an incident angle of 5° under s polarization. (B) SEM image taken at an oblique angle of 30°. The scale bar indicates 500 nm. (C) Numerically calculated reflectance spectrum under the same incident condition as that in (A). (D, E) Numerically calculated EM-field intensities of $|H|^2$ and $|E|^2$, respectively, at 559.3 nm, corresponding to a reflectance dip in (C). Approximate 40-fold EM-field intensity enhancements appear at the maxima for the incidence. Each incident wave vector k_{in} is indicated with a vertical arrow. Incident magnetic- and electric-field vectors are shown with a horizontal arrow in (D) and a coaxial circle in (E), respectively. White lines denote boundaries of the SOI nanorod and SOI/BOX interface.

nm periodicity, consisting of 205 nm diameter nanorods. Incident light traveling from air side to the metasurface was set to be s-polarized, with the electric-field vector perpendicular to the plane of incidence. The incident angle in the measurement was 5°, which approximates the normal incidence and is the smallest angle allowed in the monochromatic spectrometer. The SEM image is shown in Figure 2B, which was taken at an oblique angle of 30°. Scale bar indicates 500 nm. The SOI-nanorod metasurface was fabricated using a SOI substrate that has the top SOI layer of 200 nm thickness and the middle buried oxide (BOX) layer of 375 nm thickness. The BOX layer was produced on (100) plane of a crystalline silicon wafer of 675 μm thickness. The nanofabrication procedure is specified in the Methods.

Figure 2C shows the reflectance spectrum, numerically calculated using structural and material parameters of the measured metasurface shown in Figure 2A,B. The spectral features are fairly well-reproduced. For instance, a high reflectance band greater than 90% appears around 700 nm consistently in Figure 2A,C; the high reflectance band comes from magnetic-dipole resonance in each SOI-nanorod.[30] Also, in Figure 2A,C, relatively low reflectance regions at 500−650 nm are observed, in which several higher-order EM resonances exist close to each other.[30] In this study, we focus on FL-enhancement effect at 560−600 nm, where the resonant modes are even modes and have parabolic dispersion around 0 degrees, so that the reflectance spectra are almost independent of small incident angles less than 5°. This property can be verified in the literature (see the Figure 4).[30] We also mention that, if odd (or asymmetric) modes appear at the wavelengths of interest, the modes show prominent changes of reflectance even at a small angle of 1°; regarding the SOI-nanorod metasurface, such asymmetric modes appear around 650 nm longer than 600 nm.[30]

To clarify the resonance related to FL-intensity enhancement at a wavelength range of 560−600 nm, Figure 2D,E shows resonant electromagnetic (EM) field distributions: the magnetic- and electric-field intensities, $|\mathbf{H}|^2$ and $|\mathbf{E}|^2$, respectively, in the linear scale. The sections at the center of SOI nanorod are presented; air is above and around the nanorod, and the BOX layer is located below the nanorod. White lines indicate the boundary of the SOI nanorod. The incident wavelength was 559.3 nm, which corresponds to a reflectance dip in shown Figure 2C. The maxima of the magnetic- and electric-field intensities were 46.3 and 39.3, respectively, when the incident plane wave was set to take the intensity 1.0 for both components. Thus, the resonant EM fields are significantly enhanced. Although FL-enhancing electronic processes were already examined in detail and reported so far,[29,30] we note that the electric-field intensity, which contributes to electric-dipole transition in FL molecules, takes the maximum at the outmost surface of the SOI nanorods and contributes to the highly enhanced FL. Since the strong electric field in Figure 2E is localized very near the outmost surface of the SOI nanorods, that is, within a few nm from the outmost surface, FL-labeled targets or FL-labeled secondary Ab should be immobilized within the a-few-nanometers range to attain the large FL enhancement. Immobilization methods described later satisfy this condition.

The resonantly enhanced EM modes in all-dielectric metasurfaces were classified, and some of the EM modes were found to be suitable for large FL enhancement.[30] The EM mode in Figure 2D,E is one of the suitable modes. The resonant magnetic field in Figure 2D is strongly localized inside the SOI nanorod. The EM-field distributions indicate that the resonant mode is the first-order magnetic-field-localized guiding mode, resulting in low reflectance. The numerical method to compute the optical spectrum and EM fields is described in the Methods.

MF Setup and Molecular Immobilization. As shown in Figure 1b, the MF system was controlled by the gas pressure controller. After filling the MF paths with phosphate-buffered saline (PBS) at pH 7.4, binding molecules were flowed through to immobilize them on the metasurfaces. The binding molecules were protein AG-Cys or Cys-streptavidin. After rinsing the binding-molecule reagent, target molecules with FL labels were directly immobilized on the binding molecules. If the binding molecule used was Cys-streptavidin, the target molecules were additionally labeled with biotin; then the target was doubly labeled. When the target molecules did not have any FL label, the secondary FL-labeled Ab, which was goat-polyclonal IgG, was flowed through after rinsing the target reagent and immobilized on the target. After the target flow, the MF paths were rinsed with the PBS to remove unbound targets. More specific information is provided in the Methods.

Direct FL Detection of IgG. Figure 3 shows the results on the direct detection of IgG, which is a representative Ab and exists throughout the human body and mammal bodies. The aim of detecting IgG was to reveal capability of the metasurface sensor chips and the performance to be used as biosensors. In addition to the descriptions in the following subsections, further details related to Figure 3 can be found in Methods.

FL Measurement Configurations. The measurement setups for spectroscopic and imaging measurement are illustrated in Figure 3A,B, respectively; in the former setup, laser light source was used, and, in the latter, light-emitting-diode (LED) light source was used.

In the spectroscopic measurement, incident light at 532 nm was focused on the metasurface chip using an objective lens of

https://dx.doi.org/10.1021/acsnano.0c07722
ACS Nano XXXX, XXX, XXX−XXX

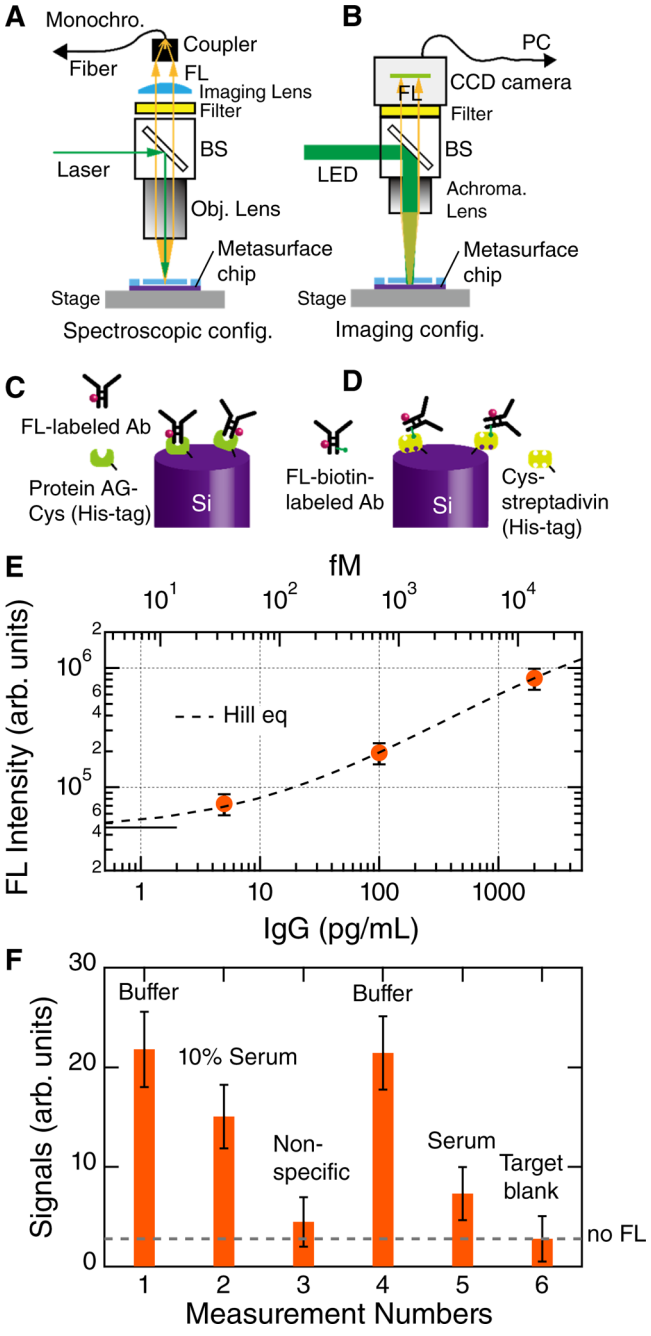

Figure 3. Direct detection of FL-labeled IgG on the metasurfaces. (A, B) FL measurement configurations for spectroscopy and imaging, respectively. (C, D) Immobilization configurations using protein AG-Cys and Cys-streptavidin as target-binding molecules, respectively. (E) Directly detected FL intensity, plotted for the target IgG concentration. The dashed curve denotes a fitted curve using the Hill equation (eq 1). (F) Effect of target-diluent buffers on FL detection. An optimized buffer for Abs was used at the measurement numbers 1 and 4; the measurements were conducted independently on different days. The effects of human serum were tested at the measurement numbers 2 and 5. A nonspecific signal is shown at the number 3. Target-blank (or background) level is also shown at the number 6, indicated by gray dashed line. The FL signals were measured at a 10 ng/mL IgG concentration, except for the number 6.

numerical aperture 0.2 and working distance 20 mm; then, the laser spot was tens of μm in diameter. The excitation laser power was set in a range from 0.15 to 0.27 mW on the metasurface chip. The metasurface area was 1200 × 600 or 2100 × 720 μm^2, so that the laser spot was smaller than the metasurface area. FL was excited at several different positions and collected using the objective lens. The collected FL went through a beam splitter (BS), a FL bandpass filter that allowed a band from 562 to 620 nm and cut the excitation laser light, and an imaging lens associated with the objective lens; then, the FL was coupled to an optical fiber, reached a monochromator, and was detected on a charge-coupled device (CCD) camera equipped with a cooling unit to reduce thermal noise. When measuring a FL spectrum, exposure time on the CCD camera was set to 20 or 25 s.

In the FL-imaging measurement, the LED spot was approximately 3 mm in diameter to allow measurement for one metasurface area at a time. The incident LED light went through a bandpass filter and was limited to a band from 515 to 540 nm; it was focused by an achromatic lens and illuminated the metasurface area. The induced FL was collected by the achromatic lens, went through a BS and a FL bandpass filter similar to that in the spectroscopic configuration, and finally reached a CCD camera that output FL images to a personal computer (PC). A FL image was taken at exposure time of 10 s. The CCD camera to output the FL images was not equipped with any cooling unit because of low-cost setup.

Direct Detection at Low Concentrations. Direct detection of goat-polyclonal IgG labeled with FL molecules, Alexa Fluor 555 (AF555), was conducted using the protein AG-Cys as shown in Figure 3C. The IgG binds to the Fc domain in the protein AG. First, the PBS was flowed through to fill the MF paths for 5 min. Second, the protein AG-Cys was diluted to 365 μg/mL with the PBS and was flowed through the MF paths with the PBS at approximately 7 μL/min for 20 min. After rinsing the MF paths with the PBS for 5 min to remove the unbound protein AG-Cys, the target AF555-labeled IgG (AF555-IgG) was flowed through at approximately 8 μL/min for 30 min. The AF555-IgG was diluted with the PBS. The final rinse to remove the unbounded AF555-IgG was done with the 150 μL PBS, and succeedingly, the MF paths were made dry with flowing N_2 gas for 10 min. The metasurface chip was set in the spectroscopic configuration (Figure 3A), and the FL was measured. Each FL spectrum was induced at 0.27 mW excitation laser power on the metasurface chip, and the CCD camera accumulated the FL signals for 25 s.

The FL intensity from the AF555-IgG is plotted for the IgG concentration in Figure 3E. The intensity was evaluated by integrating the FL spectrum in a wavelength range from 570 to 580 nm. The target concentration was defined as the concentration that the target flowed through the MF paths. The measured IgG concentration range was from 5 to 2000 pg/mL. We succeeded in detecting IgG at even a low concentration on the order of pg/mL (or tens of fM). In Figure 3E, the FL signals were fitted using the Hill equation (eq 1),[31,32] which is shown with a dashed curve and reproduce the FL-signal profile quite well. The fitted parameters were y_0 = 46000 and n = 0.58, and K_D = 108.5; the y_0 is shown with a short black line in Figure 3E, suggesting that the background level was rather high in the measurement, the n less than 1 suggests that the binding reaction is anticooperative,[33] and K_D has a dimension of ng/mL, corresponding to the half concentration in the Hill curve (see Figure S2A in the Supporting Information). We note that the error of the measured FL signals, indicated by black bars, was evaluated using several measured data, including the fluctuation of the laser light.

https://dx.doi.org/10.1021/acsnano.0c07722
ACS Nano XXXX, XXX, XXX−XXX

Since the FL-signal intensity emitted from the metasurface sensors is proportional to the number of binding targets, the FL-intensity plot for the target concentration is approximately described by the Hill equation,[31,32] which enables us to evaluate reactions between binding molecules and targets. The Hill equation is generally expressed as follows

$$y = y_0 + (S - y_0)\frac{x^n}{x^n + K_D^n} \quad (1)$$

where y denotes FL intensity, y_0 is background level in the FL measurement, S is the saturation signal intensity, x is the concentration of target, n is the degree of cooperative reaction, and K_D is the the dissociation constant. In fitting, the parameter y_0 was set and then the other parameters S, n, and K_D were optimized to minimize the least-squares. The parameters K_D and n are primarily determined by binding-bound molecule pairs; as a result, the shape of Hill curves is mainly dependent on the molecule pairs. The metasurfaces contribute to enlarging FL-signal intensity; the effect is implicitly included in a proportional parameter S. We note that eq 1 is equivalent to the so-called four-parameter logistic equation (Supporting Information S2), which is often employed to analyze immunoassays, such as ELISA.

As shown in Figure 3E, the metasurface chip detected the IgG at 5 pg/mL; the FL intensity was larger than the background level at y_0. Although it is difficult to precisely determine LOD from the measured data, the LOD is smaller than 5 pg/mL. An article[34] reported LOD for rabbit IgG using fluorophore-linked immunosorbent assay (FLISA), which was a modified ELISA. The FLISA indicated the LOD of 125 pg/mL and surface-enhanced FLISA did the LOD of 15.6 pg/mL. The surface-enhanced FLISA was an improved assay for the FLISA (that is, a kind of ELISA); however, the present metasurface sensor chip offers a quantitatively better detection performance for IgG.

We briefly mention IgG detection using a commercial ELISA kit, claiming a good performance (see the measured data descriptions in Supporting Information S3). Human-polyclonal $IgG_1\kappa$ was detected using the kit; $IgG_1\kappa$ at 0.69 ng/mL was detected, whereas $IgG_1\kappa$ at 0.23 ng/mL was not detected, at which the data was almost the same as the zero-signal level. Although there are numerous ELISA kits, the typical response based on transmission at 450 nm does not reach the surface-enhanced FLISA performance,[34] and moreover, the FLISA does not reach the present metasurface biosensor.

Test of Buffer Effects. In biosensing for target protein molecules, such as Abs and antigens, it could be an issue how to select buffer for the protein molecules since liquid biopsy such as blood contains various other biomolecules; for example, albumin and immunoglobulin. They possibly interfere with the targets and prevent the detection. To test the effects of buffers, we conducted a direct detection via biotin−streptavidin binding in Figure 3D, measured the FL images, and evaluated the signals from HiLyte 555 (HL555)-labeled human-polyclonal $IgG_1\kappa$ at 10 ng/mL under several buffer conditions, which correspond to measurement numbers 1−6 in the following: (1) we used diluent NS buffer (ab193972, Abcam, Cambridge, UK), which is a commercially available PBS-based buffer and optimized to dilute Abs, and flowed through the target solution at 7 μL/min for 30 min; (2) the FL-labeled $IgG_1\kappa$ was diluted with a buffer containing 10% human serum and 90% diluent NS, and was flowed through at 7 μL/min for 30 min; (3) to evaluate nonspecific binding on the SOI-nanorod metasurface without immobilizing Cys-streptavidin, we flowed through the target $IgG_1\kappa$ solution at 7 μL/min for 30 min, which was diluted with the NS buffer; (4) the FL-labeled $IgG_1\kappa$ was diluted with the NS buffer again on a different day from that for the measurement (1); (5) the target $IgG_1\kappa$ was diluted with 100% Human serum at 4 μL/min for 50 min; and (6) only buffers were flowed through at 7 μL/min for 30 min, without both binding Cys-streptavidin and target $IgG_1\kappa$, to determine background-signal level, which is indicated with a gray dashed line. It should be noted that the error bars primarily originate from thermal noise on the CCD camera chip, which is not equipped with a cooling unit, in the imaging configuration (Figure 3B).

From Figure 3F, we can extract several features regarding the metasurface sensors. It is evident that the metasurface sensors exhibited very high reproducibility from comparison with the measurements 1 and 4. The two data were taken on different days using different metasurface sensors and independently prepared samples. However, the observed signals are almost the same quantitatively. This is a definite advantage of the metasurface sensors because it is difficult for any other chemical sensor to ensure quantitative reproducibility in data measurement.

As a practical configuration, 10% serum buffer (the number 2) is a good option because it is always possible to make serum samples get diluted; thus, the buffer condition does not lose generality. The detected FL signals in the two configurations maintain a similar order; the FL signals in 10% serum buffer were approximately 65% of the signals in the NS buffer (numbers 1 and 4). Thus, even when a liquid biopsy includes various protein molecules besides the target, the metasurface sensors can function without substantial loss of the FL signals. This feature was obtained exploiting biotin−avidin binding between the capture molecules and the target Abs. This result using the 10% serum buffer strongly suggests that well-designed configurations for FL sensing on the metasurfaces will lead practically to sufficient performance.

As an obstacle-rich configuration, 100% serum was tested as the diluent buffer (the number 5), and definite signals that were 2.7-fold larger than those for the nonspecific condition (the number 3) were observed. Also, the signals from the full serum buffer retained 37% for signals from the 10% serum buffer. The flow rate using the full serum became 1.8-fold slower than that using the 10% serum buffer under the same pressure conditions.

Overall, it is shown that the metasurface sensors are usable for serum buffers. From a practical viewpoint of operating the MF system stably, the use of 10% serum buffer is recommended because it has low viscosity and its handling is more feasible in the MF setup, similar to the NS buffer.

We note that the used metasurface substrates can be reusable after a proper washing. To remove the immobilized protein molecules, an alkali washing liquid that does not include phosphoric acid (T-A-28, Fujiwara Scientific Co., Japan) was suitable. Going through a short-time ultrasonic-wave washing with the alkali liquid for 10 min, the substrates were washed in pure water under ultrasonic wave application. To ensure the cleanliness, additional acid washing using a solution of 96% H_2SO_4 and 30% H_2O_2 (the volume ratio 3:1) was conducted for 15 min; then a pure water rinse was done for 30 min; finally, the substrates were blown dry with dry N_2 gas.

FL Detection of p53 Ab. *Direct Detection of p53 Ab at Low Concentrations.* To examine their practical potential, the metasurface sensors were applied to p53 Ab detection. The p53 Ab, whose isotype is IgG, is a relatively recent cancer marker

https://dx.doi.org/10.1021/acsnano.0c07722
ACS Nano XXXX, XXX, XXX−XXX

expected to identify early-stage cancers.[12,35,36] We used rabbit-monoclonal p53 Ab labeled with AF555 as the target. The binding molecules were protein AG-Cys, which was used for the detection of IgG (Figure 3C). The FL spectra of the AF555-p53 Ab are shown in Figure 4A; the measured data under 0.16 mW

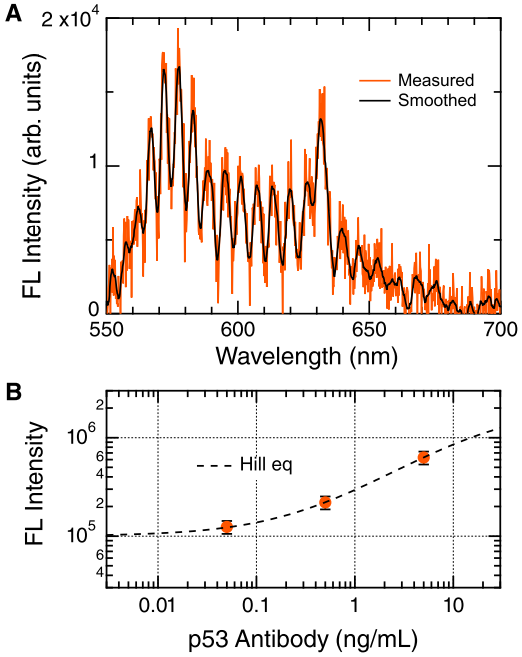

Figure 4. Direct detection of p53 Abs in FL measurement. (A) FL spectra: measured and smoothed spectra are shown with orange and black, respectively. (B) FL intensity plot for the concentration of target p53 Ab. The dashed curve denotes a fitted curve using the Hill equation (eq 1).

excitation power and 20 s exposure are shown with orange, and the smoothed data obtained using the Savitzky−Golay algorithm are shown with black. The measured interference spectrum mainly comes not from noise but from a microcavity effect inside the MF path in which the liquids were pushed out and the path was dried. To avoid being affected by the interference effect, the smoothed curve was used in the analysis as follows.

In Figure 4B, FL intensities, which were evaluated by integrating the smoothed spectra from 570 to 580 nm, are plotted for p53 Ab concentration. The p53 Ab was detected even at 50 pg/mL (or 944 fM), which is considerably lower concentration than a medical diagnosis criterion corresponding to a few ng/mL.[35] The dashed curve is a fitted curve using the Hill equation (eq 1) and reproduces the measured FL intensity. The parameters y_0, n, and K_D were 100000, 0.75, and 18.8, respectively. The qualitative property suggested by the Hill equation is similar to that suggested in the case of IgG detection, whereas the dissociation constant K_D is 5.8-fold smaller than that in Figure 3E, suggesting that the p53 Abs more easily dissociate from the binding protein AG-Cys than the IgG.

Indirect Detection of p53 Ab Including Specific and Nonspecific Test. Figure 5 shows an experimental examination for specific FL detection of p53 Abs on the metasurfaces in an indirect manner. Indirect detection is important in practically applied assay since real targets do not have any FL label. Three cases were tested simultaneously in Figure 5: (A) target mouse-monoclonal p53 Abs (black) are immobilized on the binding

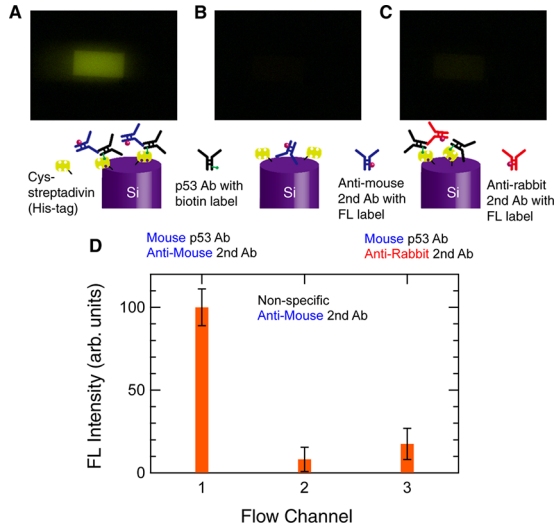

Figure 5. Comparison of specific FL detection of the p53 Ab with nonspecific FL signals. (A−C) FL images originating from specific, nonspecific, and cross-reaction immobilizations, respectively. The rectangular area correspond to the metasurfaces of 1.2 × 0.6 mm^2. The immobilization configurations are depicted below the FL images. The target was mouse p53 Ab immobilized on the SOI nanorods via biotin−avidin binding. The secondary (2nd) FL-labeled Ab was antimouse and antirabbit IgG in (A) and (C), respectively. Nonspecific binding was tested in (B). (D) FL-intensity ratio, evaluated from the FL images.

molecules of Cys-streptavidin (yellow) and the secondary antimouse AF555-IgG's (blue) bind to the target p53 Abs; (B) the target p53 Ab is not immobilized on the metasurface but the AF555-IgG is physically absorbed on a SOI nanorod, which could happen accidentally and is called nonspecific binding of FL-labeled Abs; (C) the target mouse p53 Abs are immobilized on the binding molecules and the secondary antirabbit AF555-IgG (red) binds to the target p53 Ab, which is called cross-species reaction. Note again that the target Ab is not FL-labeled. Figure 5B represents the nonspecific binding of the FL-labeled IgG on the metasurface and indicates very small FL signals.

The mouse p53 Ab at 5 μg/mL was flowed through at a flow rate of 12 ± 1 μL/min for 20 min. Further details of the procedures are given in the Methods. The FL-intensity ratio for the flow channel 1−3 was quantitatively evaluated, being shown in Figure 5D as 100 ± 11.1:8.1 ± 7.1:17.2 ± 9.1. Therefore, the specific detection is at least 10-fold more efficient than the nonspecific detection; in other words, the nonspecific detection is substantially suppressed compared to the specific detection. Also, cross-reaction between the mouse p53 Ab and the antirabbit secondary Ab in the flow channel 3 is suppressed to approximately 17% for the channel 1, suggesting that the target p53 Ab maintains the species-selective function. Overall, it was substantiated that indirect detection is achievable on the metasurface sensors.

Indirect FL Detection of CEA. A widely applied practical configuration for antigen detection is an Ab-antigen-Ab sandwich configuration. Figure 6A illustrates a sandwich-assay configuration for CEA detection. Note that the target CEA is label-free. CEA is a cancer marker, currently used for medical diagnosis.[12−14] As the binding molecules, Cys-streptavidin was first immobilized on the metasurface of the SOI-nanorod array. Then, the reaction liquid, containing biotin-labeled anti-CEA Ab, CEA, and anti-CEA Ab without any label, was flowed

https://dx.doi.org/10.1021/acsnano.0c07722
ACS Nano XXXX, XXX, XXX−XXX

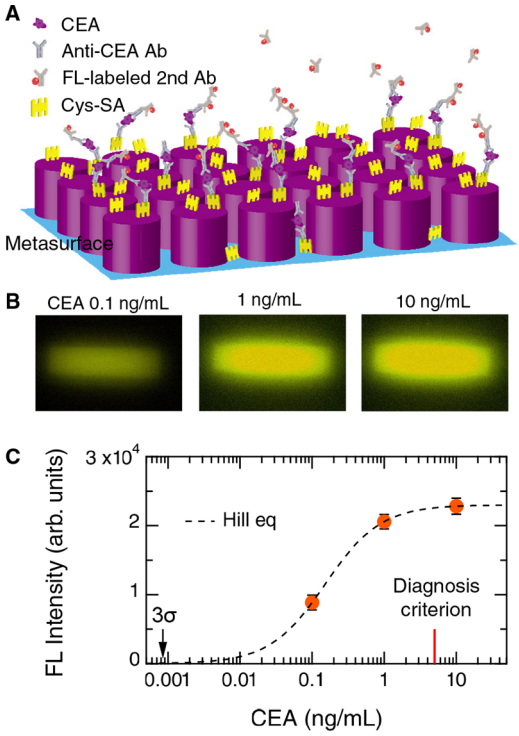

Figure 6. CEA detection in the sandwich assay. (A) Schematic of molecular configuration on the metasurface. Cys-SA denotes Cys-streptavidin. (B) FL image at 0.1, 1, and 10 ng/mL CEA concentrations from left to right, where the background was subtracted. Rectangular area corresponds to a metasurface of 2.1 × 0.72 mm^2. (C) FL-intensity plot for CEA concentration (orange closed circle) with error bar (black). The dashed curve denotes a fitted curve using the Hill equation (eq 1). The red bar indicates the medical diagnosis criterion of 5 ng/mL. The black arrow indicates the statistically estimated LOD.

through after a half-hour reaction at the room temperature (RT) of 299 K with shaking at 400 rpm. Finally, the secondary FL-labeled Ab at 100 ng/mL was flowed through and bound in part to the anti-CEA Ab. Because the secondary Abs are polyclonal, multiple binding between the secondary Abs can take place as illustrated in Figure 6A; the multiple binding yields FL amplification. After rinsing the MF path with the PBS for 10 min, we took the FL images. The total operation time was about 2 h, which can be shorten through protocol optimization. The specimen details are noted in the Methods.

FL images measured for 0.1, 1, and 10 ng/mL CEA concentrations are shown from left to right in Figure 6B; we subtracted background (that is, dark level) from each image that was taken at 2 s exposure. The rectangular metasurface area emitted FL. Note that the secondary FL-labeled Ab were also flowed outside the metasurface, but the FL intensity outside the metasurface area is substantially weaker, suggesting that nonspecific physi-absorption is quite well suppressed outside the metasurface area.

A series of FL intensities is plotted for the concentration of the target CEA in Figure 6C. The FL intensities were quantitatively evaluated analyzing FL-intensity profiles across the metasurface area in Figure 6B. Dashed curve is a fitted curve using the Hill equation (eq 1). The profile is well-reproduced and suggests that detection is highly sensitive because saturated and linearly decreasing ranges are observed. Since the current medical diagnosis criterion on CEA is 5 ng/mL indicated by a red bar, the CEA detection on the metasurface sensors is precise enough to provide quantitative results for liquid biopsies taken in hospitals and clinics. If the slope of Hill equation is needed around the diagnosis criterion, it is easy to adjust the slope by diluting the concentration of the secondary FL-labeled Abs; in Figure 6C, a rather dense concentration of 100 ng/mL was used, as the present aim is to demonstrate the CEA detection even at a low concentration range. The protocol noted in the Methods has not yet been optimized; however, the detection is expected to complete within an hour with additional optimization for the protocol.

In addition, we statistically estimated the LOD by determining 3σ (σ: standard deviation) from the zero signal. The LOD is 0.85 pg/mL (black arrow in Figure 6C), suggesting theoretically that, when the background is ideally suppressed, FL measurement enables the detection of the target CEA at extremely low concentrations.

CONCLUSIONS

Summing up several experimental results presented here, highly sensitive FL detection for IgG and p53 Ab was demonstrated in the direct configurations. The target IgG was detected at 5 pg/mL (or 34 fM), suggesting a further lower LOD. One of the practically important properties, the buffer dependence, was examined using human serum; consequently, the FL signals were obtained in a similar manner to that using PBS only. It was substantiated that the present metasurface sensor exhibited robust responses for actual liquid-biopsy-modeled buffers including human serum. In addition to the high sensitivity, the high reproducibility and quantitative detection are features of the metasurface FL sensor that are usually not ensured in other sensors. A label-free target, antigen CEA, was detected on the metasurface in the indirect configuration; the antigen detection was successfully conducted well below the medical diagnosis criterion. Comparing with the conventional ELISA that is a commercially standard for protein detection and typically takes 4 h, the present metasurface sensor offers a better sensitivity and a higher throughput less than one and a half hours. The throughput can be further improved through optimization. The metasurface substrates are reusable by washing and therefore will enable low-cost assays.

Considering all these advantages, we conclude that the present all-dielectric metasurface FL biosensor well functions as an efficient biosensor. The cancer markers were tested in this study; however, the targets are not limited to these and can be biomarkers for other diseases and infections.

METHODS

Metasurface Design and EM Computational Method. We used two designs for the experiment: one was a square array of SOI nanorods with 300 nm periodic length and 220 nm diameter and the other was that with 400 nm periodic length and 320 nm diameter. The two designs are similar to each other, though the former is relatively more optimized for the FL-enhancing experiment in the wavelength range of 570−590 nm.

To reveal the EM resonances in the metasurfaces, EM simulations were conducted. We exploited the rigorous coupled-wave analysis (RCWA) method[37] to compute optical spectra such as reflectance spectra and to evaluate the resonant EM fields. To implement numerically stable computations, the RCWA method was combined with the scattering-matrix algorithm.[38] In the computations, complex refractive index was used as material parameters. The refractive index of the crystalline silicon was taken from literature,[39] and those of BOX and air were set to be the representative values, 1.46 and 1.00027,

https://dx.doi.org/10.1021/acsnano.0c07722
ACS Nano XXXX, XXX, XXX−XXX

respectively, in the wavelength range of the present interest. A computed result is shown in Figure 2C. The prominent changes in the reflectance spectrum originate from optical resonances in the SOI nanorods. Some of the resonances play a highly positive role to enhance FL intensity;[30] one of these is shown in Figure 2D,E.

Metasurface Fabrication and Characterization. The all-dielectric metasurfaces in this study were fabricated conducting electron-beam lithography. The initial substrates were SOI substrates that have a top layer of 200 nm SOI layer and a middle layer of 375 nm BOX layer. The nanorod patterns were drawn on a negative electron-beam resist (NEB-22A, Sumitomo Chemical, Japan), using a high-resolution electron-beam-drawing instrument (JBX-6300FS, JEOL, Japan). After development the resist pattern, the SOI layer goes through dry etching in a deep reactive-ion-etching instrument for silicon (MUC-21 ASE-SRE, Sumitomo Precision Product Co., Japan) and was selectively etched down. The fabricated results are shown in Figures 1D and 2B. The SEM images were taken with a free-emission SEM instrument (SU8230, HITACHI, Japan).

The metasurface employed for Figure 3C was a square array of SOI nanorods with 300 nm periodic length and 220 nm diameter; the actual SOI nanorods were 300 nm in periodic length and 240 nm in diameter on average. The nanorod diameter was measured using the top-view SEM image, and was 9% larger than the design; however, there was no crucial deviation from the expected FL-detection results. The metasurface substrates used for Figure 3D were also fabricated following the designs of 300 nm periodic length and 220 nm diameter; the diameters of SOI nanorods were approximately 214 nm.

The metasurfaces employed for Figures 4−6 were based on the design of 400 nm periodic length and 320 nm diameter; the diameters of the fabricated SOI nanorods were 316, 330, and 315 nm, respectively. The deviation of the diameters was approximately ±3%.

MF Conditions in Operation. The MF system was regulated using a gas pressure controller (OB1, ELVEFLOW, France), which was supplied dry nitrogen gas through an external line. To control the flow rate between 5 and 10 μL/min, the output pressure for the microtubes was set to below 100 mbar in each channel. Still, a slightly higher flow rate of up to 13 μL/min sometimes occurred. In the preflow and rinses, PBS of pH 7.4 (164-25511, Wako, Japan) was used as a common buffer.

The PDMS chips were designed to have a height of 30 μm. The width of the MF path was typically 400 μm and increased to 1000 μm around the metasurface area. The mold was first fabricated on a 6 in. Si wafer with photolithography; second, PDMS liquid was spin-coated on the mold wafer and made solid with adding heat and simultaneously with pushing from the top to make the PDMS layer to be 2 mm thick; third, solid PDMS was removed from the wafer. The PDMS film of 2 mm thickness was diced into 24 squares of 19 × 19 mm^2 from the wafer size. After perforation for the in−out ports, the diced pieces were used as fabricated, without surface treatments such as hydrophilic coating. They were self-absorbed on the BOX layer of the metasurface substrates. The self-absorption was sufficient to avoid liquid leak from the MF paths. Other examples of PDMS chips and the fabrication processes are also seen in the literature.[6,9]

Biosamples and Their Manipulation. The target AF555-IgG in Figure 3E was goat-polyclonal and antirabbit, labeled prior to shipping (ab150078, Abcam). To dilute the target IgG, we used a commercial buffer (diluent NS) with pH 7.4 that was optimized to dilute Abs. The diluent NS is based on PBS, and includes bovine serum albumin and ethylenediaminetetraacetic acid. To immobilize the target IgG on the metasurface, the protein AG-Cys (PRO1001, Click Biosystems, TX) was used for binding molecules. The His-tag on the protein AG-Cys is able to bind the outermost nm-thick oxide layer of the SOI nanorods; a similar effect was reported for His-tag streptavidin.[33]

When testing the coexisting protein effect in human serum (12181201, Cosmo Bio Co., Japan) in Figure 3F, we prepared a buffer containing 10% serum and 90% diluent NS. This was partially because we intended to avoid clogging the MF paths, though the serum did not clog the MF paths even when we used 100% serum as buffer. The target IgG$_1\kappa$ was human-polyclonal (ab206202, Abcam), FL-labeled using a commercial kit (LK14, Dojindo Molecular Technologies, Rockville, MD); the FL molecule was HyLite 555 (HL555), which has almost the same light absorption and FL-emission bands to those of AF555. Then the HL555-labeled IgG$_1\kappa$ was biotinylated using a biotin-labeling kit (LK03, Dojindo Molecular Technologies). These kits added the labels to the NH$_2$ bases of IgG$_1\kappa$. Thus, the target was doubly labeled. In the FL measurement, we did not observe any substantial loss or negative effect, coming from the double labeling.

The doubly labeled IgG$_1\kappa$ was immobilized on Cys-streptavidin via the His-tag (PRO1005, Click Biosystems), which was diluted by the PBS to 20 μg/mL and flowed at approximately 10 μL/min for 25 min before the flow of the target IgG$_1\kappa$.

The p53 Ab labeled with AF555 in Figure 4 was antimutant and rabbit-monoclonal (ab210717, Abcam). The target Abs were immobilized using the protein AG-Cys, similar to the case in Figure 3C. After the final rinse with the PBS, the MF paths were made dry by N$_2$ gas flow, and the metasurface chip was measured in the spectroscopic configuration (Figure 3A).

The target p53 Ab in Figure 5 was mouse-monoclonal (ab16465, Abcam) and was additionally biotinylated using the same labeling kit as that used for IgG$_1\kappa$ in Figure 3F. The Cys-streptavidin was first immobilized on the metasurfaces to bind the target. The Cys-streptavidin was diluted with the PBS to 20 μg/mL and flowed at 11−12 μL/min for 30 min. After rinsing with the PBS for 10 min, we flowed the diluted target p53 Ab, the diluent NS, and the diluted target p53 Ab for 20 min, in the flow channels 1−3, respectively; the flow rate was 11−13 μL/min. The channel 2 was used to measure the blank (or no target configuration). The dilution of the target p53 Ab was conducted with the diluent NS, and the target concentration was set to 5 μg/mL. After the channels were rinsed with the PBS for 15 min, the secondary Abs of goat-polyclonal AF555-IgG at a 100 ng/mL concentration were flowed through at 11−12 μL/min for 30 min; the secondary Ab was diluted with the diluent NS. In the channels 1 and 2, the AF555-IgG was antimouse (ab150114, Abcam), whereas, in the channel 3, the AF555-IgG was antirabbit (ab150078, Abcam); these Abs were employed to test the cross-reaction between different species. After rinsing the channels with the PBS for 10 min, we measured the FL images presented in Figure 5A−C.

For the CEA detection in Figure 6, the Cys-streptavidin was flowed through at 20 μg/mL for 50 min to prepare the binding molecules. The anti-CEA Ab (Abcam, ab229074) was rabbit-monoclonal and the target CEA (ab742, Abcam) was native protein. A part of the anti-CEA Ab was biotinylated using the labeling kit, the same as for the IgG$_1\kappa$ detection. The sandwich complexes of biotin-labeled anti-CEA Ab, target CEA, and anti-CEA Ab were formed under incubation at rt and 400 rpm for 60 min; the concentrations of the two-type anti-CEA Ab were adjusted to 100 ng/mL using the diluent NS, and the CEA concentrations of 30, 3, and 0.3 ng/mL were prepared using the diluent NS. Each Ab and CEA reagent to form the sandwich complexes was 100 μL, so that each sandwich cocktail had a total volume of 300 μL. Eventually, the target CEA concentrations were 10, 1, and 0.1 ng/mL. After the incubation, the cocktail was flowed at approximately 10 μL/min for 28 min. Flowing through washing buffer (in ELISA kit, ab195215, Abcam) for 10 min and rinsing with the PBS for 10 min, the secondary AF555-IgG of 100 ng/mL was flowed for 30 min at the rate of 9 μL/min in each channel. The AF555-IgG was goat-polyclonal and antirabbit (ab150078, Abcam). After rinsing the MF paths with the PBS for 10 min, we conducted the FL imaging.

Optical Measurement and Analysis. Reflectance measurement for the all-dielectric metasurfaces was conducted using a monochromatic spectrometer (V-7200, JASCO, Japan), which is able to measure reflectance at the incident angle of 5° and larger angles. Since the spectrometer requires a large-area metasurface to conduct the measurement, we prepared a metasurface with approximately 2 × 2 mm^2 dimension through the electron-beam lithography. The reflectance spectrum in Figure 2A was measured on the large-area metasurface employing the spectrometer.

The spectrometer was also employed to measure transmittance of FL-labeled IgG and p53 Ab. From the transmittance at 280 and 555 nm, we can evaluate light absorption by the FL molecules and Abs and consequently figure out the FL-labeling ratio, that is, the ratio of number of bound FL molecules to a Ab. The labeling ratio of the

https://dx.doi.org/10.1021/acsnano.0c07722
ACS Nano XXXX, XXX, XXX−XXX

HL555-IgG was found to be approximately 7.5 and that of the IgG-AF555 was approximately1.5. The procedure to figure out the labeling ratio is described in the Supporting Information S4.

The configurations in the FL measurement are illustrated in Figure 3A,B. The Savitzky−Golay algorithm took 21 neighbor points, which meant the 21st-order approximation, and smoothed the measured data with the second-order polynomial shown in Figure 4A. This data analysis was conducted on commercial data-analysis graph-production software.

ASSOCIATED CONTENT

Supporting Information

The Supporting Information is available free of charge at https://pubs.acs.org/doi/10.1021/acsnano.0c07722.

Detailed technical information: (S1) photograph of the MF setup; (S2) the Hill equation and 4-parameter logistic equation; (S3) ELISA result for IgG; (S4) evaluation of FL-labeling ratio of the HL555-IgG and AF555-IgG (PDF)

AUTHOR INFORMATION

Corresponding Author

Masanobu Iwanaga − *Research Center for Functional Materials, National Institute for Materials Science (NIMS), Tsukuba 305-0044, Japan;* orcid.org/0000-0002-8930-6940; Email: iwanaga.masanobu@nims.go.jp

Complete contact information is available at: https://pubs.acs.org/10.1021/acsnano.0c07722

Notes

The author declares the following competing financial interest(s): Most of the contents in this article were filed in a PCT Patent (PCT/JP2020/041153).

ACKNOWLEDGMENTS

We thank Naoki Ikeda and Jun Matsuzawa for technical assistance in the nanofabrication of metasurfaces and Saki Ishihara for technical assistance in the FL detection. This study was partially supported by JSPS KAKENHI Grant No. JP17H01066, by the HPCI system research project (IDs: hp180107, hp190037), which enabled us to use the supercomputers at Cyberscience Center, Tohoku University, and by the fourth midterm and M-CUBE projects in NIMS. Nanofabrication procedures were conducted in part at the Namiki Foundry and Nanofabrication Platform in NIMS.

REFERENCES

(1) Yu, N.; Capasso, F. Flat Optics with Designer Metasurfaces. *Nat. Mater.* **2014**, *13*, 139−150.

(2) Jahani, S.; Jacob, Z. All-Dielectric Metamaterials. *Nat. Nanotechnol.* **2016**, *11*, 23−36.

(3) Genevet, P.; Capasso, F.; Aieta, F.; Khorasaninejad, M.; Devlin, R. Recent Advances in Planar Optics: From Plasmonic to Dielectric Metasurfaces. *Optica* **2017**, *4*, 139−152.

(4) Liang, H.; Martins, A.; Borges, B.-H. V.; Zhou, J.; Martins, E. R.; Li, J.; Krauss, T. F. High Performance Metalenses: Numerical Aperture, Aberrations, Chromaticity, and Trade-Offs. *Optica* **2019**, *6*, 1461−1470.

(5) Kuznetsov, A. I.; Miroshnichenko, A. E.; Brongersma, M. L.; Kivshar, Y. S.; Luk'yanchuk, B. Optically Resonant Dielectric Nanostructures. *Science* **2016**, *354*, aag2472.

(6) Yavas, O.; Svedendahl, M.; Dobosz, P.; Sanz, V.; Quidant, R. On-a-Chip Biosensing Based on All-Dielectric Nanoresonators. *Nano Lett.* **2017**, *17*, 4421−4426.

(7) Tittl, A.; Leitis, A.; Liu, M.; Yesilkoy, F.; Choi, D.-Y.; Neshev, D. N.; Kivshar, Y. S.; Altug, H. Imaging-Based Molecular Barcoding with Pixelated Dielectric Metasurfaces. *Science* **2018**, *360*, 1105−1109.

(8) Myszka, D. G.; He, X.; Dembo, M.; Morton, T. A.; Goldstein, B. Extending the Range of Rate Constants Available from BIACORE: Interpreting Mass Transport-Influenced Binding Data. *Biophys. J.* **1998**, *75*, 583−594.

(9) Zhou, J.; Tao, F.; Zhu, J.; Lin, S.; Wang, Z.; Wang, X.; Ou, J.-Y.; Li, Y.; Liu, Q. H. Portable Tumor Biosensing of Serum By Plasmonic Biochips in Combination with Nanoimprint and Microfluid. *Nanophotonics* **2019**, *8*, 307−316.

(10) Zhu, J.; Wang, Z.; Lin, S.; Jiang, S.; Liu, X.; Guo, S. Low-Cost Flexible Plasmonic Nanobump Metasurfaces for Label-Free Sensing of Serum Tumor Marker. *Biosens. Bioelectron.* **2020**, *150*, 111905.

(11) Morote, J.; Raventós, C. X.; Lorente, J. A.; Lopez-Pacios, M. A.; Encabo, G.; de Torres, I.; Andreu, J. Measurement of Free PSA in the Diagnosis and Staging of Prostate Cancer. *Int. J. Cancer* **1997**, *71*, 756−759.

(12) Kumamoto, K.; Ishida, H.; Kuwabara, K.; Amano, K.; Chika, N.; Okada, N.; Ohsawa, T.; Kumagai, Y.; Ishibashi, K. Clinical Significance of Serum Anti-p53 Antibody Expression Following Curative Surgery for Colorectal Cancer. *Mol. Clin. Oncol.* **2017**, *7*, 595−600.

(13) Ushigome, M.; Shimada, H.; Miura, Y.; Yoshida, K.; Kaneko, T.; Koda, T.; Nagashima, Y.; Suzuki, T.; Kagami, S.; Funahashi, K. Changing Pattern of Tumor Markers in Recurrent Colorectal Cancer Patients Before Surgery to Recurrence: Serum p53 Antibodies, CA19−9 and CEA. *Int. J. Clin. Oncol.* **2020**, *25*, 622−632.

(14) Takehara, K.; Takehara, Y.; Ueyama, S.; Kobayashi, T. A Case of Stercoral Colitis with Marked Elevation of Serum Carcinoembryonic Antigen. *Clin. Case Rep.* **2020**, *8*, 734−738.

(15) Giljohann, D. A.; Mirkin, C. A. Drivers of Biodiagnostic Development. *Nature* **2009**, *462*, 461−464.

(16) Rissin, D. M.; Kan, C. W.; Campbell, T. G.; Howes, S. C.; Fournier, D. R.; Song, L.; Piech, T.; Patel, P. P.; Chang, L.; Rivnak, A. J.; Ferrell, E. P.; Randall, J. D.; Provuncher, G. K.; Walt, D. R.; Duffy, D. C. Single-Molecule Enzyme-Linked Immunosorbent Assay Detects Serum Proteins at Subfemtomolar Concentrations. *Nat. Biotechnol.* **2010**, *28*, 595−599.

(17) Kim, S. H.; Iwai, S.; Araki, S.; Sakakihara, S.; Iino, R.; Noji, H. Large-Scale Femtoliter Droplet Array for Digital Counting of Single Biomolecules. *Lab Chip* **2012**, *12*, 4986−4991.

(18) Luan, J.; Seth, A.; Gupta, R.; Wang, Z.; Rathi, P.; Cao, S.; Derami, H. G.; Tang, R.; Xu, B.; Achilefu, S.; Morrissey, J. J.; Singamaneni, S. Ultrabright Fluorescent Nanoscale Labels for The Femtomolar Detection of Analytes with Standard Bioassays. *Nat. Biomed. Engineer.* **2020**, *4*, 518−530.

(19) Touahir, L.; Galopin, E.; Boukherroub, R.; Gouget-Laemmel, A. C.; Chazalviel, J.-N.; Ozanam, F.; Szunerits, S. Localized Surface Plasmon-Enhanced Fluorescence Spectroscopy for Highly-Sensitive Real-Time Detection of DNA Hybridization. *Biosens. Bioelectron.* **2010**, *25*, 2579−2585.

(20) Zhou, L.; Ding, F.; Chen, H.; Ding, W.; Zhang, W.; Chou, S. Y. Enhancement of Immunoassay's Fluorescence and Detection Sensitivity Using Three-Dimensional Plasmonic Nano-Antenna-Dots Array. *Anal. Chem.* **2012**, *84*, 4489−4495.

(21) Zhang, W.; Ding, F.; Li, W.-D.; Wang, Y.; Hu, J.; Chou, S. Y. Giant and Uniform Fluorescence Enhancement over Large Areas Using Plasmonic Nanodots in 3D Resonant Cavity Nanoantenna by Nanoimprinting. *Nanotechnology* **2012**, *23*, 225301.

(22) Choi, B.; Iwanaga, M.; Miyazaki, H. T.; Sugimoto, Y.; Ohtake, A.; Sakoda, K. Overcoming Metal-Induced Fluorescence Quenching on Plasmo-Photonic Metasurfaces Coated by a Self-Assembled Monolayer. *Chem. Commun.* **2015**, *51*, 11470−11473.

(23) Iwanaga, M.; Choi, B.; Miyazaki, H. T.; Sugimoto, Y. The Artificial Control of Enhanced Optical Processes in Fluorescent Molecules on High-Emittance Metasurfaces. *Nanoscale* **2016**, *8*, 11099−11107.

(24) Kinkhabwala, A.; Yu, Z.; Fan, S.; Avlasevich, Y.; Müllen, K.; Moerner, W. E. Large Single-Molecule Fluorescence Enhancements Produced by a Bowtie Nanoantenna. *Nat. Photonics* **2009**, *3*, 654−657.
(25) Schmelzeisen, M.; Zhao, Y.; Klapper, M.; Müllen, K.; Kreiter, M. Fluorescence Enhancement from Individual Plasmonic Gap Resonances. *ACS Nano* **2010**, *4*, 3309−3317.
(26) Fu, C.-C.; Ossato, G.; Long, M.; Digman, M. A.; Gopinathan, A.; Lee, L. P.; Gratton, E.; Khine, M. Bimetallic Nanopetals ror Thousand-Fold Fluorescence Enhancements. *Appl. Phys. Lett.* **2010**, *97*, 203101.
(27) Punj, D.; Mivelle, M.; Moparthi, S. B.; van Zanten, T. S.; Rigneault, H.; van Hulst, N. F.; García-Parajó, M. F.; Wenger, J. A Plasmonic 'Antenna-in-Box' Platform for Enhanced Single-Molecule Analysis at Micromolar Concentrations. *Nat. Nanotechnol.* **2013**, *8*, 512−516.
(28) Iwanaga, M.; Choi, B. Heteroplasmon Hybridization in Stacked Complementary Plasmo-Photonic Crystals. *Nano Lett.* **2015**, *15*, 1904−1910.
(29) Iwanaga, M. *Plasmonic Resonators: Fundamentals, Advances, and Applications*; Pan Stanford Publishing: Singapore, 2016; Chapter 5.
(30) Iwanaga, M. All-Dielectric Metasurfaces with High-Fluorescence-Enhancing Capability. *Appl. Sci.* **2018**, *8*, 1328.
(31) Gesztelyi, R.; Zsuga, J.; Kemeny-Beke, A.; Varga, B.; Juhasz, B.; Tosaki, A. The Hill Equation and the Origin of Quantitative Pharmacology. *Arch. Hist. Exact Sci.* **2012**, *66*, 427−438.
(32) Neubig, R. R.; Spedding, M.; Kenakin, T.; Christopoulos, A. International Union of Pharmacology Committee on Receptor Nomenclature and Drug Classification. XXXVIII. Update on Terms and Symbols in Quantitative Pharmacology. *Pharmacol. Rev.* **2003**, *55*, 597−606.
(33) Irrera, A.; Leonardi, A. A.; Di Franco, C.; Lo Faro, M. J.; Palazzo, G.; D'Andrea, C.; Manoli, K.; Franzò, G.; Musumeci, P.; Fazio, B.; Torsi, L.; Priolo, F. New Generation of Ultrasensitive Label-Free Optical Si Nanowire-Based Biosensors. *ACS Photonics* **2018**, *5*, 471−479.
(34) Furtaw, M. D.; Steffens, D. L.; Urlacher, T. M.; Anderson, J. P. A Near-Infrared, Surface-Enhanced, Fluorophore-Linked Immunosorbent Assay. *Anal. Chem.* **2013**, *85*, 7102−7108.
(35) Ochiai, H.; Ohishi, T.; Osumi, K.; Tokuyama, J.; Urakami, H.; Seki, S.; Shimada, A.; Matsui, A.; Isobe, Y.; Murata, Y.; Endo, T.; Ishii, Y.; Hasegawa, H.; Matsumoto, S.; Kitagawa, Y. Reevaluation of Serum p53 Antibody as a Tumor Marker in Colorectal Cancer Patients. *Surg. Today* **2012**, *42*, 164−168.
(36) Yokomizo, H.; Yoshimatsu, K.; Yano, Y.; Okayama, S.; Sakuma, A.; Satake, M.; Yamada, Y.; Matsumoto, A.; Fujimoto, T.; Usui, T.; Yamaguchi, K.; Shiozawa, S.; Shimakawa, T.; Katsube, T.; Kato, H.; Naritaka, Y. Clinical Significance of Serum p53 Antibody Measurement in Colorectal Cancer Patients. *Gan To Kagaku Ryoho* **2016**, *43*, 1301−1303 (in Japanese).
(37) Li, L. New Formulation of the Fourier Modal Method for Crossed Surface-Relief Gratings. *J. Opt. Soc. Am. A* **1997**, *14*, 2758−2767.
(38) Li, L. Formulation and Comparison of Two Recursive Matrix Algorithm for Modeling Layered Diffraction Gratings. *J. Opt. Soc. Am. A* **1996**, *13*, 1024−1035.
(39) Palik, E. D. *Handbook of Optical Constants of Solids II*; Academic: San Diego, USA, 1991.

https://dx.doi.org/10.1021/acsnano.0c07722
ACS Nano XXXX, XXX, XXX−XXX